JOM
https://doi.org/10.1007/s11837-026-08740-5

In Situ Synchrotron X-ray Diffraction Study of Flash Austenitization and Process Design Insights in Medium-Manganese Steels for Energy Applications

BOWEN ZOU ,[1,5] MATHIAS ZAPF,[2] THEA KANNENBERG,[3,4] DANIEL SCHNEIDER,[3,4] YIXU WANG,[1] XIAO SHEN,[1] ULRICH PRAHL,[2] and WENWEN SONG[1]

1.—Department of Granularity of Structural Information in Materials Engineering, Institute of Materials Engineering, University of Kassel, Mönchebergstraße 7, 34125 Kassel, Germany. 2.—Faculty of Materials Science and Technology, Institute of Metal Forming, Technische Universität Bergakademie Freiberg, Bernhard-von-Cotta-Straße 4, 09599 Freiberg, Germany. 3.—Institute of Digital Materials Science (IDM), Karlsruhe University of Applied Sciences (HKA), Moltkestraße 30, 76133 Karlsruhe, Germany. 4.—Institute for Applied Materials (IAM-MMS), Karlsruhe Institute of Technology (KIT), Straße am Forum 7, 76131 Karlsruhe, Germany. 5.—e-mail: bowen.zou@uni-kassel.de

Medium-manganese steels (MMnSs) are promising materials for energy infrastructure because tailoring their multiphase microstructures and austenite stability can improve failure resistance. Flash austenitization (FA) rapidly forms austenite while limiting prior austenite grain coarsening and substitutional solute homogenization, but its short-time kinetics remain insufficiently quantified. In the present study, two initial states of an Fe-6Mn-1.5Si-1Cr-0.3Mo-0.05Nb-0.2C (wt.%) MMnS, obtained by austenite reversion treatment (ART), were heated at 100°C/s to 850°C, 900°C, or 950°C and held isothermally while phase evolution was tracked by dilatometry-integrated in situ synchrotron X-ray diffraction. Neither passing the reference A_{c3} determined under slow heating nor reaching the FA temperature was sufficient to achieve near-complete austenitization, defined as $f_\alpha < 1$ wt.%. Holding times of approximately 8 s, 4 s, and 2 s were required at 850°C, 900°C, and 950°C, respectively. Despite differences in the initial austenite fraction, morphology, and Mn enrichment, both ART states showed comparable transformation progress during rapid heating. Increasing the FA temperature shifted more transformation into the heating ramp, thereby reducing the residual bcc fraction at the beginning of holding and changing the austenitization path during holding. These results demonstrate that rapid heating and isothermal holding form a kinetically coupled flash austenitization process.

INTRODUCTION

The infrastructure required for safe energy storage and transportation imposes strict demands on structural steels, which must resist failure in hydrogen-containing environments and at low temperatures. In hydrogen energy systems, steels used for pipelines and pressure vessels are exposed to environments where hydrogen ingress can reduce their ductility and fracture toughness.[1–3] This makes hydrogen embrittlement and hydrogen-assisted cracking a central concern for the safe operation and lifetime design of these systems. Meanwhile, cryogenic storage and transport systems, such as those for liquefied natural gas and liquid hydrogen, require base materials and welded joints with sufficient low-temperature toughness, often assessed by impact testing at − 196°C.[4,5] Under these conditions, brittle fracture becomes more likely, and the welded heat-affected zone

(Received June 11, 2026; accepted August 25, 2026)

Published online: 11 September 2026

(HAZ) is often a critical region.[6] Taken together, hydrogen and cryogenic services demand steels with a balanced combination of strength, toughness, and weldability, together with microstructures designed to resist hydrogen-induced degradation and low-temperature fracture. In this context, medium-manganese steels (MMnSs) have attracted increasing interest as structural materials for energy-related infrastructure, owing to their multiphase microstructures and austenite stability, which can be tailored through alloying and heat treatment to improve strength, toughness, and resistance to hydrogen-assisted degradation.[7–10] Their weld HAZ response has also been studied in resistance spot welding and laser welding, where optimized welding schedules and short post-weld thermal cycles have been proposed to control local hardening and improve joint performance.[6,11–13]

In MMnSs, the microstructural design strategy centers on a multiphase structure comprising austenite, ferrite, and/or martensite, allowing strength, ductility, and toughness to be tuned through phase fractions, morphology, and austenite stability. During austenite reversion treatment (ART), Mn partitions into reverted austenite; however, complete Mn homogenization is kinetically limited during short holding times because of slow Mn diffusion. Thus, local Mn inhomogeneity can remain after ART. Atom probe tomography (APT) studies have reported core-shell Mn gradients in reverted austenite in MMnSs,[14] while studies on triplex MMnSs have shown local C and Mn segregation at phase boundaries, indicating that nanoscale Mn heterogeneity is strongly processing-dependent.[15] Local Mn enrichment can increase austenite stability and therefore provides a route to tune deformation behavior and the balance among strength, ductility, and toughness.[16,17] For hydrogen-related service, such chemical heterogeneity can also be used as a designed feature. Sun et al.,[18] for example, introduced a high density of Mn-rich zones, which increased local austenite stability and hydrogen trapping, slowed hydrogen-assisted microcrack growth, and improved hydrogen resistance without sacrificing strength and ductility in high-strength steels. Austenite stability is also important for cryogenic service, where retained austenite stability has been linked to cryogenic impact toughness in a low-C MMnS.[19] Therefore, the mechanical performance of MMnSs for energy applications is closely linked to the heat treatment path and phase transformation kinetics, because they determine the austenite fraction, grain size, austenite stability, and Mn heterogeneity.

The concept of flash austenitization (FA) can be traced back to the rapid austenitizing treatments described by Grange,[20] in which steel is rapidly heated through the critical temperature range between A_{c1} and A_{c3}, with no holding or only a very short holding time, followed by immediate cooling. These cycles are typically produced by induction or resistance heating, with heating rates from $\sim$ 10°C/s to several hundred °C/s.[21–23] The austenitization temperature can therefore be reached within seconds, reducing high-temperature exposure during heating and holding. This limited exposure restricts interface migration and diffusion, thereby suppressing austenite grain coarsening.[21–23] Subsequent rapid-heating studies have reported finer prior austenite grains and martensitic substructures after quenching, with greater refinement at higher heating rates.[24–26] These results support the basic rationale of FA, indicating that austenite formation can occur within a very short high-temperature interval while limiting prior austenite grain coarsening.

For MMnSs, FA is particularly relevant because short high-temperature exposure can promote rapid austenite formation while limiting substitutional Mn diffusion and redistribution. As a result, Mn heterogeneity generated during ART is less likely to be fully homogenized during subsequent austenitization, even after the austenite transformation is complete. Previous studies on MMnSs showed that rapid heating at 100°C/s enabled fast austenite formation and C partitioning while retaining Mn-related chemical heterogeneity in post-ART or tempered microstructures.[27,28] These findings support a processing route in which ART first introduces Mn segregation and gradients, followed by FA to form austenite rapidly, limit prior austenite grain coarsening, and preserve part of the inherited Mn heterogeneity. However, this route requires transformation kinetics that allow full austenitization within a very short time.

A previous in situ synchrotron X-ray diffraction (SYXRD) study showed that the heating rate and initial microstructure can be used to control the austenitization path during rapid heating.[29] Increasing the heating rate from 0.25°C/s to 100°C/s shifted austenitization to higher temperatures and changed the phase-dissolution sequence, including the coupled evolution of ferrite, cementite, and austenite. This is particularly relevant for MMnSs after ART, where ferrite, retained austenite, and martensite coexist before FA and Mn-related chemical heterogeneity may affect local transformation kinetics. However, holding conditions during FA are still often chosen empirically,[22,24,25,27] because quantitative evidence on the seconds-scale required for full austenitization remains limited. In particular, it remains unclear whether full austenitization can be achieved without holding, or within only a few seconds, and how this depends on austenitization temperature, holding time, and the initial ART microstructure. To address this gap, the present work directly quantifies phase evolution during FA after ART using dilatometry-integrated in situ SYXRD. FA temperature (850°C, 900°C, and 950°C), holding time, and two initial ART states (ART700-10 and ART700-60) are varied at a fixed heating rate of 100°C/s to

determine the minimum time required for full austenitization and clarify the effects of initial microstructure and holding parameters on transformation kinetics. Based on these results, a transformation-kinetics-based processing window is established to guide the design of FA treatment for MMnSs.

MATERIALS AND METHODS

Materials and Processing

A MMnS with a nominal composition of Fe-6Mn-1.5Si-1Cr-0.3Mo-0.05Nb-0.2C (wt.%) was produced by vacuum induction melting and cast into a 75-kg ingot with dimensions of ~ 140 mm × 140 mm × 450 mm. Nb and Mo were added to refine the prior austenite grain size and retard austenite grain growth during subsequent heat treatments.[30] The ingot was homogenized at 1250°C for 5 h and hot forged between 1200°C and 900°C into billets of ~ 70 mm × 70 mm × 900 mm. The billets were hot rolled in nine passes to 2.0 mm and then cold rolled to 1.5 mm without interpass annealing; no obvious surface defects or edge cracks were observed after cold rolling. Specimens for subsequent experiments were wire-cut from the cold-rolled (CR) sheets, with the 10-mm dimension parallel to the rolling direction. The specimen geometry for dilatometry and dilatometry-integrated in situ SYXRD measurements was 10 mm × 4 mm × 1.5 mm.

The chemical composition was measured by pulse discrimination analysis-optical emission spectrometry (PDA-OES) at Georgsmarienhütte Gruppe and is listed in Table I. The critical transformation temperatures A_{c1}, A_{c3}, and M_s of the CR condition were determined by dilatometry using a DIL 805 A/D in quenching mode at the Institute of Metal Forming, TU Bergakademie Freiberg. These temperatures correspond to the start and finish of austenite formation during heating, and the martensite start temperature during cooling under the applied dilatometry conditions. The cycle consisted of heating to 1100°C at 3°C/min, holding for 30 min, and quenching to room temperature at 140°C/s with the gas valve fully open. Figure 1a shows the corresponding dilatation curves and the transformation temperatures, with A_{c1} = 618°C, A_{c3} = 776°C, and M_s = 235°C. According to the Stahl-Eisen-Prüfblätter (SEP) 1681 standard, the critical temperatures were determined using the lever rule, with transformation progress (TF) values of 0.01 and 0.99 as thresholds for the start and finish of transformation, respectively. In addition to the main austenite formation range, the dilatation curve shows a second high-temperature inflection between 865°C and 1058°C.

Based on the dilatometry results, two ART conditions were applied in a salt bath (GS 540/R2 salt) at 700°C for 10 min (ART700-10) and 60 min (ART700-60), followed by air cooling to room temperature. These ART conditions served as the initial microstructural states for the subsequent FA experiments. The CR sample and ART-treated conditions were characterized by electron backscatter diffraction (EBSD) and ex situ SYXRD, as described in the "Initial Microstructure Characterization" section. In situ SYXRD during rapid heating at 100°C/s and isothermal holding was performed using a DIL 805 A/D at beamline P07B-EH1, as detailed in the "Dilatometry-Integrated In Situ Synchrotron X-ray Diffraction" section. Figure 1b schematically summarizes the ART routes and subsequent in situ FA measurements.

Initial Microstructure Characterization

Microstructural characterization of the CR condition and the two ART conditions (ART700-10 and ART700-60) was performed using EBSD and ex situ SYXRD to characterize phase constitution, morphology, and crystallographic features at room temperature. EBSD was performed using a Helios 5 Hydra plasma-focused ion beam scanning electron microscope (PFIB-SEM) equipped with a CMOS-based EBSD detector (Oxford Instruments). Specimens were mechanically ground with SiC papers up to 4000 grit, polished with 3 μm and 1 μm diamond suspensions, and finally electropolished in universal electrolyte A2 at 40 V for 10–12 s using an electrolyte flow rate setting of 18. EBSD data were acquired at 20 kV, 13 nA, a working distance of 10 mm, and a 0.04 μm step size. Data acquisition and post-processing were conducted using AZtec and AZtecCrystal (Oxford Instruments, Version 3.3), respectively. EBSD maps were used to quantify the distributions of the face-centered cubic (fcc) and body-centered cubic (bcc) phases, grain morphology, and grain size in the CR and ART states. Grain size analysis used a 15° high-angle grain boundary criterion, and grain size was evaluated as the arithmetic mean equivalent circular diameter (ECD). Ex situ SYXRD patterns at room temperature were obtained for the CR and ART conditions using the same P07 beamline setup as described for the in situ experiments in the "Dilatometry-

Table I. Chemical composition (in wt.%) of the investigated MMnS

MMnS	Fe	Mn	Si	Cr	Mo	Nb	C	P	S	N
wt.%	balance	5.920	1.560	1.070	0.330	0.052	0.210	0.004	0.004	0.005

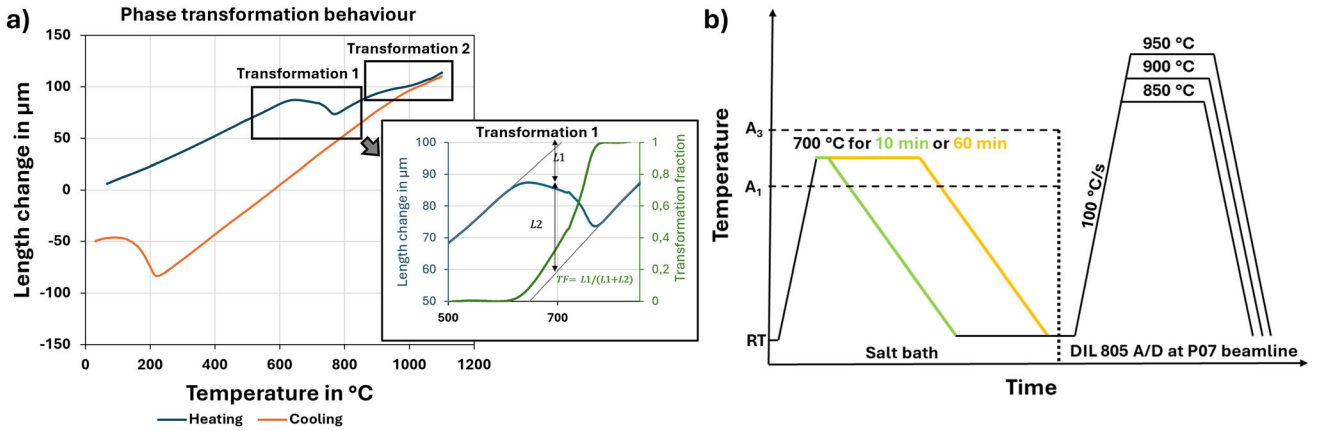

Fig. 1. (a) Dilatation curve of the cold-rolled MMnS steel and the enlarged views of the transformation regions used to determine A_{c1}, A_{c3} and M_s using the DIL 805A/D. (b) Schematic illustration of the austenite reversion treatment (ART) routes at 700°C for 10 min and 60 min, followed by air cooling, which were used as the initial states for the subsequent in situ FA experiments (FA: flash austenitization, RT: room temperature).

Integrated In Situ Synchrotron X-ray Diffraction" section. The 2D diffraction images were azimuthally integrated over 0° to 360° to obtain 1D intensity profiles using Pydidas.[31] The fcc (γ) and bcc (α) reflections within a 2θ range of 3.5° to 8.5° were identified using crystallographic reference data from the Crystallography Open Database. The diffraction profiles were used for phase identification and to determine the initial peak positions and lattice parameters before in situ heating.

To directly examine local Mn partitioning in the initial ART states, correlative scanning transmission electron microscopy-transmission Kikuchi diffraction-energy-dispersive X-ray spectroscopy (STEM-TKD-EDS) characterization was performed on FIB-prepared transmission electron microscopy (TEM) lamellae from ART700-10 and ART700-60 in the PFIB-SEM instrument. STEM bright-field images were recorded at 30 kV and 50 pA with a working distance of 4.65 mm. TKD scans were acquired over selected correlative regions of approximately 1 × 1 μm^2 with a step size of 5 nm. TKD data were acquired at 30 kV and 3.2 nA using a 52° pre-tilted lamella holder, with the SEM stage tilted to 35°, corresponding to an effective specimen tilt of 17°, and a working distance of 5 mm. To enable reliable spatial correlation between the phase map and chemical analysis, the forescatter detector (FSD) signal from the EBSD system was used to enhance microstructural contrast and locate the fcc/bcc regions for subsequent EDS line scans. EDS line scans were then acquired from the same regions of the lamellae at 20 kV, 1.6 nA, and a working distance of 4.65 mm. The TKD phase maps were used to identify the fcc and bcc regions, while the EDS line profiles were used to compare the local Mn distribution across adjacent fcc and bcc regions. TKD and EDS data acquisition was performed using AZtec, and TKD post-processing was conducted using AZtecCrystal.

Dilatometry-Integrated In Situ Synchrotron X-ray Diffraction

Dilatometry-integrated in situ SYXRD was carried out during FA treatment at beamline P07B-EH1 (PETRA III, DESY, Hamburg, Germany).[32] The experiments were performed in transmission geometry using a monochromatic beam (beam energy about 87.1 keV, wavelength 0.14235 Å) with a beam size of 1 mm × 0.7 mm. This beam size was selected to enable short acquisition times while sampling a sufficiently large gauge volume and maintaining adequate diffraction statistics. FA treatment was conducted using a dilatometer (DIL 805 A/D) from TA Instruments integrated at P07B-EH1, as shown in Fig. 2. The chamber had X-ray-transparent windows for the incident and diffracted beams, and the sample was induction-heated while held between quartz push rods. Temperature was monitored and controlled via a thermocouple spot-welded to the specimen surface near the X-ray-illuminated volume. The chamber was evacuated and backfilled with Ar to protect the sample and limit oxidation during rapid heating and isothermal holding. Diffraction patterns (Debye-Scherrer rings) were recorded continuously using a PerkinElmer 2D area detector, covering up to 2θ = 8.5°. Detector geometry was calibrated with a LaB_6 powder standard (NIST SRM 660C) to determine the beam center, detector tilt and rotation, and sample-to-detector distance.

For the in situ SYXRD during FA, two initial microstructural states were prepared by ART at 700°C for 10 min (ART700-10) and 60 min (ART700-60). Specimens from each state were mounted in the DIL 805 A/D and measured throughout the thermal cycle. As shown in Fig. 1b, samples were heated at 100°C/s to FA temperatures of 850°C, 900°C, or 950°C and held isothermally for 5 min to monitor microstructural evolution and phase transformation. Rapid heating was recorded in fast-acquisition mode at 10 patterns s^{-1},

Fig. 2. Experimental setup for in situ SYXRD during FA at beamline P07B-EH1 (PETRA III, DESY). Left: overview of the DIL 805 A/D mounted in the beamline hutch with the incident beam path and the 2D detector. Right: the chamber showing the specimen positioned between quartz push rods, with the incident beam passing through the gauge section in transmission geometry.

corresponding to a time resolution of 0.1 s, with the beam continuously on. This mode started 30 s before heating, covered the heating stage, and continued for 2 min after reaching the FA temperature. Acquisition was then switched to a single pattern every 5 s for the remaining holding period to reduce the 2D detector load and data volume. During FA, the DIL 805 A/D recorded the time-temperature profile, whereas the 2D detector stored diffraction data only as sequential image numbers without time stamps referenced to the start of heat treatment. Because the acquisition-mode switch introduced time offsets, the diffraction time axis was reconstructed by synchronizing the dilatometer time-temperature data with the 2D detector sequence using a Python script provided by beamline P07. The script assigned each image number an absolute time and corresponding sample temperature, producing a consistent time-temperature-diffraction dataset for further analysis.

The recorded 2D diffraction images were batch-processed using azimuthal integration over 0°–360° to obtain 1D diffraction profiles with Pydidas.[31] Quantitative analysis of the 1D diffraction data was performed by Rietveld refinement using MAUD software (version 2.99993)[33,34] to obtain the Rietveld-refined weight fractions of the fcc (γ) and bcc (α) phases, which are reported in wt.%. Phase identification and lattice parameter tracking during heating and holding were performed using the characteristic fcc (γ) and bcc (α) reflections within a 2θ range of 3.5° to 8.5°, with reference crystallographic data taken from the Crystallography Open Database. The instrumental line broadening was determined from a LaB_6 standard measured under the same detector geometry. The LaB_6 reference pattern was refined to determine the instrumental peak-profile contribution by fitting the background and instrument broadening parameters, including Caglioti, asymmetry, and Gaussian parameters, in the MAUD instrument model. The resulting instrumental profile parameters were then fixed for refinement of the investigated steel specimens, with only the background, scale factors, and lattice parameters of the fcc and bcc phases being refined. The refinement quality was evaluated using the weighted profile R factor (R_{wp}), the expected R factor (R_{exp}), and χ^2, where $\chi^2 = (R_{wp}/R_{exp})^2$. In MAUD, $\sqrt{\chi^2}$ is represented as sig, which corresponds to the goodness of fit (R_{wp}/R_{exp}). For correctly estimated experimental uncertainties, R_{wp} approaches R_{exp} and χ^2 approaches 1, whereas $\chi^2 < 1$ indicates overestimated uncertainties or overparameterization.[35] Since a fixed upper limit for χ^2 is not generally valid and can change with counting statistics, background level, and systematic effects,[35] the refinements were also verified by graphical comparison of the observed and calculated patterns, including the difference curve, to confirm that the selected phase and profile models adequately describe the measured data.

RESULTS

Microstructure Characterization of the Investigated MMnS in the Cold-Rolled and ART Conditions

The microstructures of the investigated MMnS under CR conditions and after ART at 700°C for 10 min or 60 min, followed by air cooling to room temperature, were characterized using EBSD and ex situ SYXRD. Figure 3a, b, and c shows the corresponding EBSD phase maps of the CR, ART700-10, and ART700-60 conditions, respectively, while Fig. 3d shows the corresponding room-temperature ex situ SYXRD profiles. The EBSD measurements provide local information on phase distribution, grain morphology, grain boundary misorientation, and grain size. The grain size distributions for all studied conditions are provided as supplementary Fig. S-1. The quantitative microstructural parameters obtained from EBSD and Rietveld refinement of the SYXRD data are summarized in Table II.

The CR sample (Fig. 3a) shows an almost fully bcc microstructure, with an EBSD-indexed bcc phase

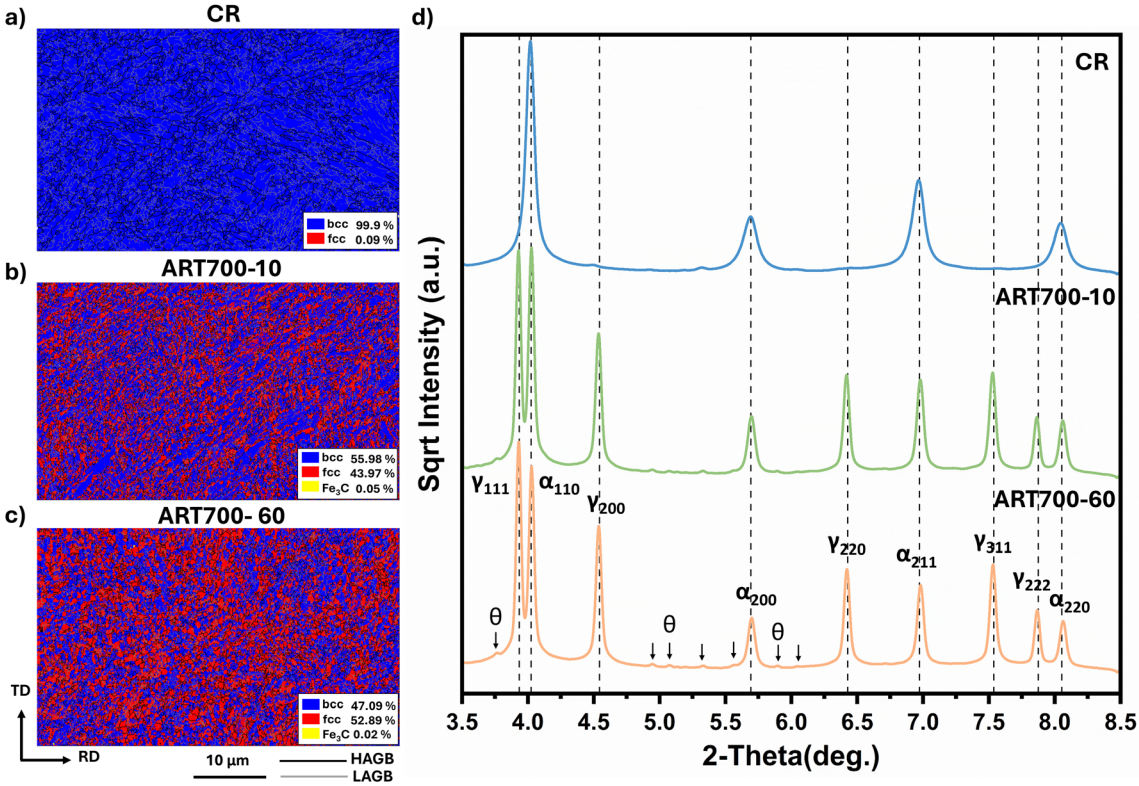

Fig. 3. Microstructural analysis of the investigated MMnS in the cold-rolled (CR) condition and after austenite reversion treatment (ART) at 700°C. (a) EBSD phase map of the CR condition, (b) EBSD phase map after ART700-10 (700°C for 10 min, air-cooled), and (c) EBSD phase map after ART700-60 (700°C for 60 min, air-cooled). Blue, red, and yellow represent the bcc (α), fcc (γ), and cementite (θ) phases, respectively. (d) Ex situ SYXRD profiles of the three conditions.

Table II. Microstructural parameters determined from EBSD and ex situ SYXRD for the investigated conditions. γ and α denote fcc (austenite) and the bcc (ferrite/martensite-related) phases, respectively. ECD denotes the equivalent circular diameter determined from EBSD. The SYXRD phase fractions are Rietveld-refined weight fractions

	EBSD						Ex situ SYXRD			
	Phase fraction (%)		Grain size (ECD, μm)		Grain boundary fraction (%)		Phase fraction (wt.%)		Lattice parameter (Å)	
Sample	γ	α	γ	α	LAGB	HAGB	γ	α	γ	α
CR	0.09	99.91	–	0.68 ± 0.63	54.86	45.14	0.12 ± 0.07	99.88 ± 0.91	3.588	2.871
ART700-10	43.97	55.98	0.30 ± 0.18	0.42 ± 0.39	49.60	50.40	56.71 ± 0.69	43.29 ± 0.57	3.596	2.865
ART700-60	52.89	47.09	0.35 ± 0.23	0.44 ± 0.34	49.55	50.45	64.58 ± 0.65	35.42 ± 0.43	3.597	2.864

fraction of 99.91%, and an fcc phase fraction of only 0.09%. Most bcc grains are elongated by rolling, although locally equiaxed grains a few micrometers in size occur between them. After ART at 700°C for 10 min and air cooling to room temperature (Fig. 3b), the microstructure changes to a refined fcc/bcc dual-phase state, with submicrometer- to micrometer-scale grains. A small fraction of cementite-related indexed regions is detected, but should be interpreted with caution because it is close to the EBSD phase-indexing limit. The fcc grains are mainly equiaxed and are located predominantly along grain and subgrain boundaries of the elongated bcc regions inherited from the CR state, while part of the bcc phase still retains the rolling-induced elongated morphology. Extending ART at 700°C to 60 min (Fig. 3c) produces a predominantly equiaxed dual-phase microstructure, with slightly coarser fcc grains and a much weaker elongated bcc morphology. Thus, ART transforms the deformation-induced, bcc-dominated CR microstructure into a fine fcc/bcc dual-phase microstructure with a higher

austenite fraction and a moderate reduction in low-angle grain boundaries (LAGBs) (Table II). The EBSD-indexed fcc fraction increases from 43.97% after 10 min to 52.89% after 60 min.

The ex situ SYXRD profiles in Fig. 3d confirm the phase constitution identified by EBSD for the CR, ART700-10, and ART700-60 conditions. The dashed vertical reference lines indicate the calculated peak positions of the main fcc and bcc reflections, based on the incident X-ray wavelength and reference lattice parameters of a_{fcc} = 3.591 Å and a_{bcc} = 2.867 Å from the Crystallography Open Database. The calculation procedure is provided as supplementary Note S-1. These calculated positions were used for peak assignment, whereas the lattice parameters and phase fractions listed in Table II were obtained from Rietveld refinement.

In the CR condition (blue curve in Fig. 3d), the diffraction profile is dominated by bcc (α) reflections (e.g., α_{110}, α_{200}, α_{211}), while no distinct fcc (γ) reflections are observed. This result is consistent with the EBSD phase map, which shows an almost fully bcc microstructure in the CR state. The bcc (α) peaks in the CR condition are shifted slightly to lower 2θ values compared with the reference positions, corresponding to a larger refined bcc lattice parameter of 2.871 Å (Table II). This expanded bcc lattice parameter is attributed to the combined diffraction signals from deformed ferrite and body-centered-tetragonal (bct) martensite. C supersaturation in martensite, high dislocation density, and residual elastic strain contribute to the peak shift and broadening.[36–38]

After ART at 700°C, distinct γ reflections (γ_{111}, γ_{200}, γ_{220}, γ_{311}, γ_{222}) appear in both ART700-10 and ART700-60, confirming the formation and retention of austenite after air cooling. The refined austenite lattice parameter is 3.596 Å for ART700-10 and 3.597 Å for ART700-60, as shown in Table II, respectively. Both values are slightly larger than the reference fcc lattice parameter, and the value after 60 min ART is only marginally higher. This is consistent with solute redistribution between α and γ during ART, especially C enrichment of austenite, because interstitial C expands the fcc lattice.[39,40] However, the small change in the average austenite lattice parameter suggests that extending ART from 10 min to 60 min mainly increases the retained austenite fraction. C partitioning at 700°C can proceed relatively rapidly toward local equilibrium, whereas long-range Mn redistribution is much slower. Thus, austenite reversion and growth during prolonged ART holding are primarily governed by interface migration.[41–43] The increase in retained austenite fraction with longer ART holding is more pronounced than the change in the average austenite lattice parameter. In addition, weak cementite-related reflections are visible under ART conditions, consistent with the small cementite-related indexed regions observed by EBSD.

Compared with ART700-10, ART700-60 shows stronger γ reflections and weaker α reflections, indicating a higher austenite fraction after prolonged ART holding. This trend is confirmed by Rietveld refinement, with the γ fraction increasing from 56.71 ± 0.69 wt.% in ART700-10 to 64.58 ± 0.65 wt.% in ART700-60 (Table II). The same trend is also observed by EBSD, although the absolute austenite fractions obtained by EBSD are lower than those obtained by SYXRD. This difference is expected because EBSD provides local surface-based area fractions, whereas SYXRD probes a much larger volume of material and yields bulk-averaged Rietveld-refined weight fractions. In addition, EBSD can underestimate finely divided or highly strained retained austenite due to step-size limits, interaction volume, and indexing quality.[44,45] Despite this difference in absolute values, both methods consistently show that extending the ART holding time promotes austenite reversion. Such an increase in retained austenite fraction with increasing ART holding time has been widely reported for MMnSs and is commonly attributed to continued austenite reversion and ongoing elemental partitioning during ART holding.[17,41,46,47]

To characterize local phase-specific Mn partitioning in the ART initial states, correlative STEM-TKD-EDS was performed on FIB-prepared lamellae from ART700-10 and ART700-60, as shown in Fig. 4. The TKD phase maps resolve submicrometer-scale fcc regions embedded in or adjacent to bcc regions, consistent with the refined fcc and bcc dual-phase microstructure observed by EBSD and ex situ SYXRD. Within the selected local TKD scan areas, the indexed phase fractions are 89.87% bcc and 10.13% fcc for ART700-10 and 87.28% bcc and 12.72% fcc for ART700-60. These values should not be interpreted as representative area fractions, because the TKD scans cover only selected correlative local regions. The EDS line scans were taken across adjacent fcc and bcc regions identified from the TKD maps. In both ART states, the Mn concentration is higher in the fcc regions than in the adjacent bcc regions. The phase-specific averages calculated from the selected EDS line profiles are approximately 7.9 wt.% Mn in fcc and 3.9 wt.% Mn in bcc for ART700-10 and approximately 9.3 wt.% Mn in fcc and 3.8 wt.% Mn in bcc for ART700-60. These local line scan values show stronger Mn enrichment of austenite after 60 min ART, while the average Mn concentrations in the sampled bcc regions remain comparable. The values are used for a semi-quantitative comparison of the selected phase regions and are not treated as bulk phase compositions. The measurements therefore establish the phase-specific Mn distribution that forms the chemical starting condition for the subsequent FA treatments.

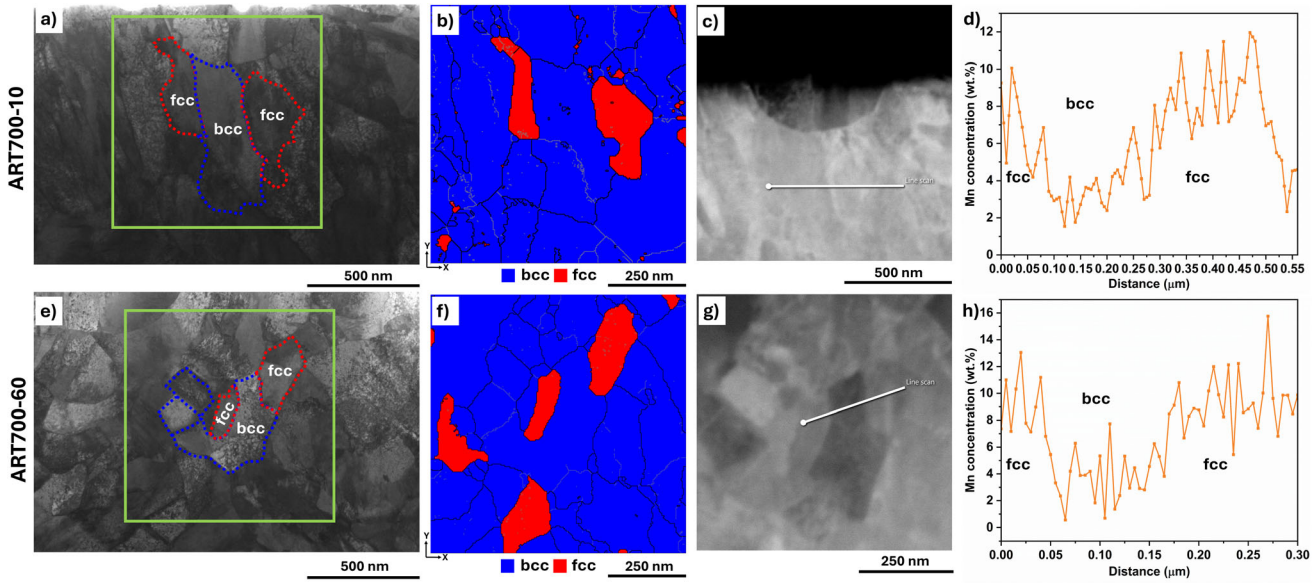

Fig. 4. Correlative STEM-TKD-EDS characterization of local Mn distribution in the ART states using FIB-prepared lamellae. The upper row shows ART700-10 and the lower row shows ART700-60. (a, e) STEM image of the analyzed regions of the lamellae. The green boxes indicate the areas selected for TKD analysis, while representative fcc and bcc grains are outlined by red and blue dotted lines, respectively. (b, f) TKD phase maps showing bcc and fcc regions. Blue and red denote bcc and fcc, respectively. (c, g) FSD images showing the EDS line-scan positions across adjacent fcc and bcc regions. (d, h) Corresponding Mn concentration profiles along the line scans.

Dilatometric Analysis of Transformation Temperatures During Flash Austenitization (FA)

The FA treatment was conducted in a dilatometer to monitor temperature- and time-dependent length changes during rapid heating, isothermal holding, and subsequent cooling. Because fcc and bcc phases have different specific volumes, the dilatation signal provides complementary information on phase transformations throughout the thermal cycle. Transformation temperatures are governed by both the initial microstructure, including chemical composition, phase fractions, and prior deformation state, and the process parameters, such as heating rate, which alter the temperatures at which transformations are detected. Here, the initial conditions were adjusted by the preceding ART, producing two starting states, ART700-10 and ART700-60. Therefore, the dilatometry-derived critical transformation temperatures were determined during rapid heating at 100°C/s for both ART conditions.

Figure 5a shows that both ART-processed conditions exhibit a two-step transformation behavior during rapid heating to 950°C. For ART700-10, the two transformation stages start at approximately 687°C and 799°C, whereas the corresponding temperatures for ART700-60 are approximately 690°C and 789°C. Similar transformation temperatures indicate that the start of transformation is only weakly affected by the initial ART state. From the dilatation curves, the finish temperatures of the main austenite formation process are also similar, approximately 875°C for ART700-10 and 879°C for ART700-60, indicating that both ART states transform over a comparable temperature range during rapid heating to 950°C. However, these temperatures should be regarded as dilatometry-derived finish temperatures of bcc-to-fcc transformation, not as direct proof of full austenitization. Therefore, the completion of austenitization during FA needs further verification by in situ SYXRD results. The high-temperature transformation segment (transformation 2 as shown in Fig. 5a) is more pronounced in ART700-10 than in ART700-60. This behavior is consistent with the higher bcc phase fraction in ART700-10, which provides a larger phase fraction available for austenite transformation during rapid heating. In contrast, ART700-60 already contains a higher retained austenite fraction before FA, so the additional austenite formation during heating is reduced. These dilatometry results show that the two ART initial states transform at similar temperatures but differ in the amount of transformation occurring during rapid heating.

Length reduction during isothermal holding at the FA temperature (Fig. 5b) further indicates incomplete austenitization of the fcc/bcc dual-phase microstructure during rapid heating. At the beginning of the isothermal holding, the length change (ΔL) decreases rapidly and is followed by a slight, continuous decrease. In some cases, even a small expansion is observed, which may be due to a background signal associated with the dilatometer setup. This overlapping effect in the ΔL signal makes it difficult to determine the transformation completion directly from the raw dilatation curve. The relative length-change rate was therefore

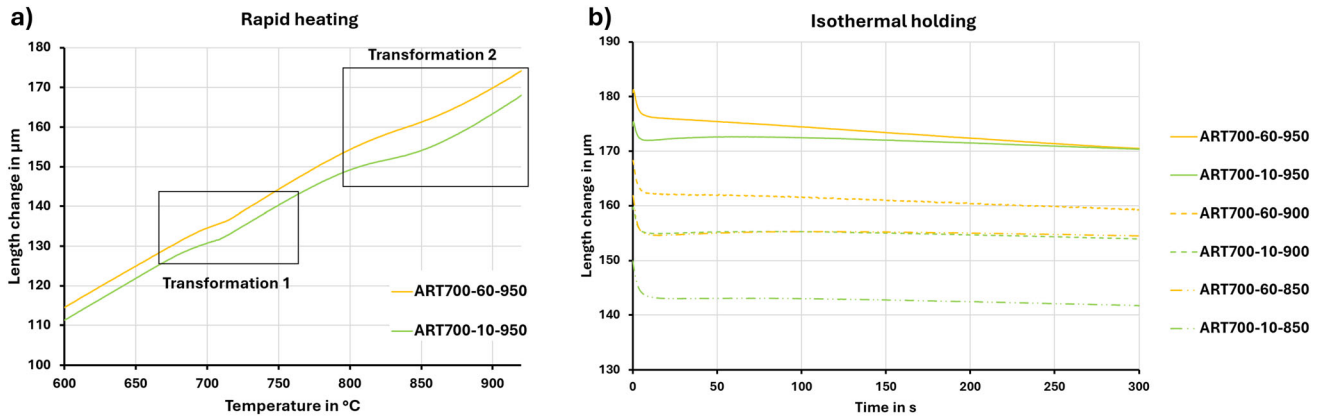

Fig. 5. Dilatation behavior of FA during (a) rapid heating with 100°C/s up to 950°C for both initial microstructural states, ART700-10 and ART700-60, (b) dilatation behavior during isothermal holding at the selected austenitization temperatures.

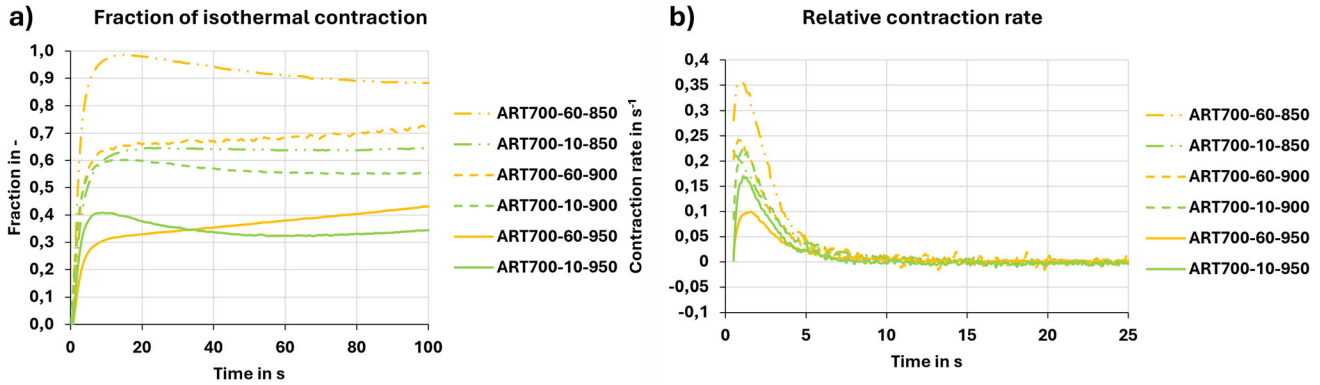

Fig. 6. Kinetics of length change during isothermal transformation showing (a) the relative fraction of isothermal contraction and (b) the corresponding relative contraction rate.

calculated after smoothing the data with an 11-point moving average, according to Eq. 1.

$$\frac{\Delta f}{\Delta t} = \frac{f_{i+1} - f_i}{t_{i+1} - t_i} \quad (1)$$

where f_i is the relative length-change fraction at data point i, and t_i is the corresponding time.

As shown in Fig. 6, the relative isothermal contraction increases rapidly at the start of holding and then either reaches a local maximum followed by a slight decrease or gradually changes into a slower continuous contraction. Larger contraction is observed at lower FA temperatures. This trend is compatible with a larger remaining bcc-to-fcc transformation contribution, but the dilatation signal also contains overlapping non-transformation contributions. Likewise, the higher contraction fractions measured for ART700-60 at 850°C and 900°C cannot be assigned uniquely to austenite formation. Phase-resolved analysis is therefore required, as discussed in the "Microstructural Evolution and Phase Transformation Behavior During Flash Austenitization Revealed by In Situ SYXRD" section. The corresponding relative contraction rates (Fig. 6b) are high at the beginning of holding and decrease rapidly within the first few seconds. For all conditions, the rate approaches a low, nearly steady level within ~ 25 s, showing that the main isothermal transformation is largely completed within this time range.

From these dilatation rate data, the end time of the isothermal austenite transformation was estimated and is summarized in Table III. For ART700-60 at 950°C, a reliable end time could not be determined because of the smooth transition to continuous contraction. The estimated dilatometric end time decreases with increasing FA temperature and with longer ART holding before FA. Because the residual bcc fraction at the start of holding also changes with FA temperature and initial ART state, these end times do not isolate the intrinsic isothermal transformation rate. The shorter end times after ART700-60 are consistent with its higher initial austenite fraction and the smaller amount of residual bcc requiring transformation during isothermal holding.

Table III. Estimated end time of the isothermal transformation during FA holding from the contraction rate curves (n.d., not determined)

FA temperature	ART700-10	ART700-60
850°C	22 s	13 s
900°C	15 s	10 s
950°C	8 s	n.d.

Microstructural Evolution and Phase Transformation Behavior During Flash Austenitization Revealed by In Situ SYXRD

Figure 7 summarizes the in situ SYXRD results for ART700-10 during rapid heating in FA at 100°C/s to 850°C, 900°C, and 950°C. Figure 7a, c, and e presents the waterfall plots of diffraction profiles over 2θ = 3.5°–6.6°, focusing on temperature ranges near the reference A_{c1} (618°C) and A_{c3} (776°C) determined by slow-heating dilatometry in the "Materials and Processing" section. Figure 7b, d, and f shows the enlarged views of the α_{110} and γ_{111} reflections to more clearly track the bcc (α) phase to fcc (γ) phase transformation during rapid heating. In all three FA thermal cycles, the room temperature diffraction profiles (Fig. 7a, c and e) contain both bcc and fcc reflections, including γ_{111}, γ_{200}, γ_{220} and α_{110}, α_{200}, together with weak cementite peaks. This confirms that the three ART700-10 specimens had comparable initial-phase compositions before FA, with the corresponding phase fractions summarized in Supplementary Table S-I. On heating, the bcc and fcc reflections shift continuously to lower 2θ values, consistent with lattice expansion. Below the reference A_{c1}, these shifts mainly reflect thermal expansion and rearrangement of deformed structures, with no substantial bcc-to-fcc transformation. Above A_{c1}, the α reflections gradually lose intensity, marking the onset and progress of austenite formation during rapid heating. Near A_{c3}, the α intensity drops sharply, indicating the transformation of a large fraction of bcc to fcc. Nevertheless, weak α reflections remain after passing A_{c3} and persist until the target FA temperatures are reached, showing that the bcc-to-fcc transformation is incomplete during the rapid heating ramp even at 850°C, 900°C, or 950°C. Cementite-related reflections progressively weaken, consistent with dissolution, with only very weak signals remaining at the end of the ramp.

Quantitative phase analysis further confirms that austenitization is incomplete at the end of rapid heating. For the rapid heating to 850°C (Fig. 7a and b), α reflections remain clearly visible at the end of the heating ramp, especially the α_{110} reflection in the enlarged view. The Rietveld-refined phase fractions at 850°C are f_γ = 90.51 ± 0.54 wt.% and f_α = 9.49 ± 0.39 wt.%, confirming that a considerable bcc fraction remains. A similar trend is observed for rapid heating to 900°C (Fig. 7c and d). Although the α_{110} intensity is strongly reduced compared with the 850°C condition, a weak α peak remains detectable at 900°C, corresponding to f_γ = 96.56 ± 1.74 wt.% and f_α = 3.44 ± 0.59 wt.%. Even for rapid heating to 950°C (Fig. 7e and f), residual α reflections are still detectable at the end of the heating stage, with f_γ = 97.62 ± 0.80 wt.% and f_α = 2.38 ± 0.48 wt.%. In this work, $f_\alpha \leq 1$ wt.% (i.e., $f_\gamma \geq 99$ wt.%) was used as a quantitative threshold for near-complete bcc-to-fcc transformation during austenitization. This 1 wt.% threshold does not imply a bcc-free fully austenitic microstructure. It provides a consistent threshold for comparing the extent of near-complete bcc-to-fcc transformation among the different FA conditions. The use of a 1% residual-bcc criterion is consistent with transformation analyses in which the start and finish of a transformation are commonly defined using 1% and 99% transformed fractions, respectively.[48] In addition, when the residual bcc fraction approaches ~ 1 wt.%, the α_{110} reflection becomes weak and partially overlaps with the tail of the γ_{111} reflection, making quantitative interpretation increasingly sensitive to background subtraction and refinement uncertainty. Therefore, the 1 wt.% threshold was selected as a conservative criterion for process comparison, to avoid overinterpreting very small Rietveld-refined phase fractions.[49] Using the threshold, none of the three FA treatments reaches near-complete bcc-to-fcc transformation during rapid heating alone, even at 950°C.

Figure 8 shows the in situ SYXRD response of ART700-10 during isothermal holding after rapid heating in FA, with time (t) = 0 defined as the moment the target FA temperature is reached. The waterfall plots in Fig. 8a, c, and e over 2θ = 3.5° to 6.6° track the diffraction profile evolution during 300-s holding time, while Fig. 8b, d, and f enlarges the α_{110} region to monitor residual bcc. Selected phase fractions are summarized in Table S-I. The lower initial α_{110} intensity at 900°C and 950°C than at 850°C agrees with the smaller α fraction remaining after rapid heating, as shown in Fig. 7 and Table S-I. At 850°C (Fig. 8a and b), the α_{110} intensity decreases strongly within the first few seconds. The α fraction drops from 9.49 ± 0.39 wt.% at t = 0 to 0.85 ± 0.13 wt.% after 8 s, falling below the defined threshold $f_\alpha \leq 1$ wt.%, while f_γ increases to 99.15 ± 1.97 wt.%. At 900 and 950°C (Fig. 8c–f), the same trend occurs, but the time required to reach the near-completion criterion is shorter. At 900°C, f_α decreases from 3.44 ± 0.59 wt.% to 0.87 ± 0.17 wt.% after 4 s, with f_γ = 99.12 ± 0.69 wt.%. At 950°C, f_α reaches 0.78 ± 0.15 wt.% after only 2 s, giving the shortest completion time among the three FA temperatures.

In addition to changes in intensity, the position of the residual α_{110} reflection also shifts during isothermal holding. When comparing the 850°C, 900°C, and 950°C conditions, the residual α_{110} peak

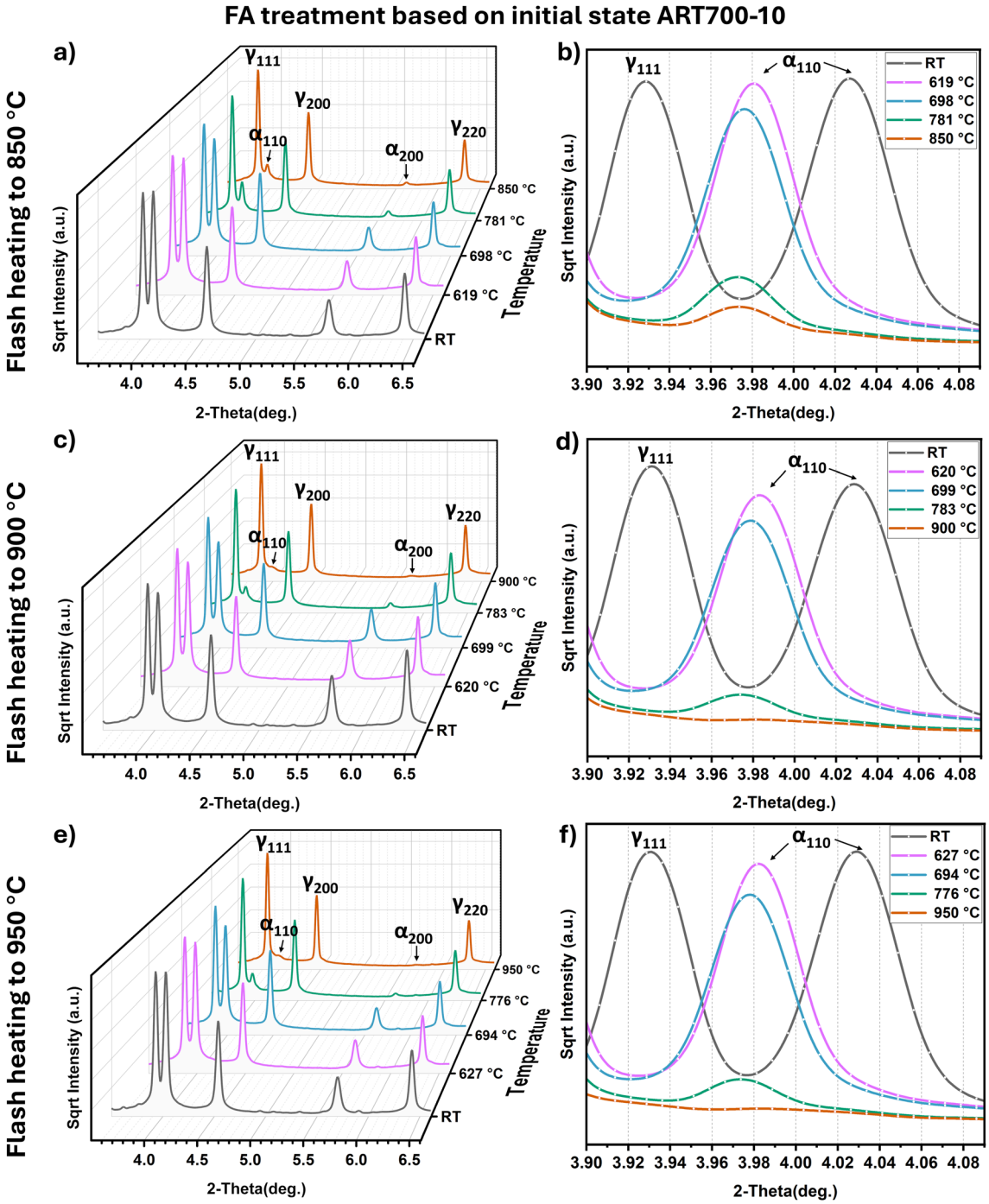

Fig. 7. In situ SYXRD results show microstructural evolution and phase transformation of ART700-10 during rapid heating at 100°C/s from room temperature (RT) to FA temperatures of 850°C (a, b), 900°C (c, d), and 950°C (e, f). (a, c, and e) Waterfall plots of the diffraction profiles in the 2θ range 3.5 to 6.6°, highlighting the evolution of bcc (α) and fcc (γ) reflections during heating. (b, d, and f) Enlarged views around γ_{111} and α_{110}.

is located slightly toward higher 2θ at higher FA temperatures, although thermal expansion alone would shift diffraction peaks toward lower 2θ. This indicates that the lattice parameter of the small residual α fraction is affected not only by temperature but also by changes in local composition, e.g., elemental partitioning of C and Mn and strain state during holding.

Figure 9 shows the in situ SYXRD results for ART700-60 during rapid heating in FA at 100°C/s to 850°C, 900°C, and 950°C. The room-temperature profiles contain both α and γ reflections, confirming an fcc/bcc dual-phase initial microstructure across all three FA cycles, with comparable initial phase fractions as listed in Supplementary Table S-II. During rapid heating, the α and γ reflections shift to lower 2θ values due to thermal expansion, while the

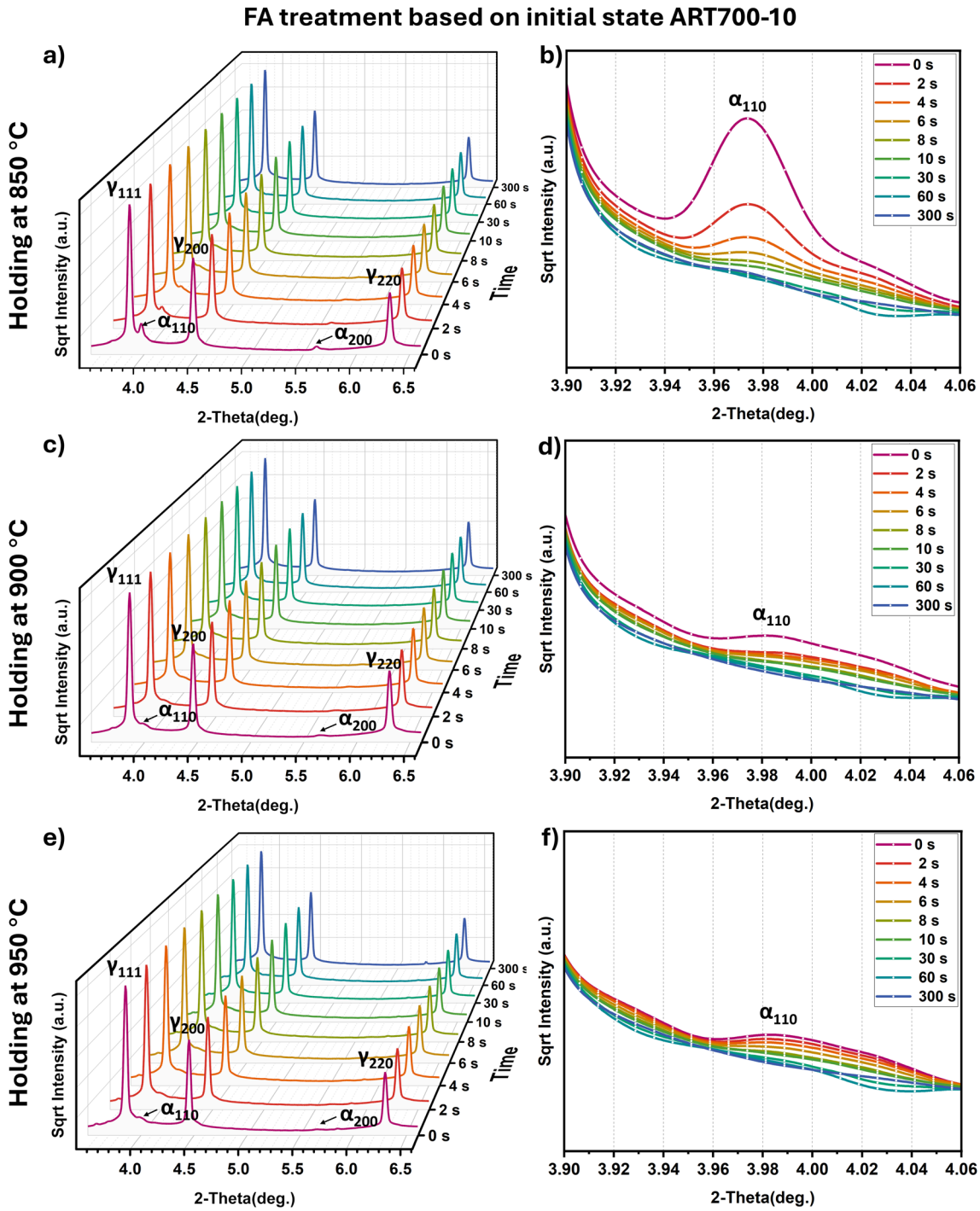

Fig. 8. In situ SYXRD results of ART700-10 during isothermal holding after rapid heating in FA to 850°C (a, b), 900°C (c, d), and 950°C (e, f). Waterfall plots (a, c, e) show the time-dependent evolution of α and γ reflections during holding and the enlarged views (b, d, f) highlight the progressive decrease of the residual α_{110} reflections.

α peak intensity decreases progressively, especially near the reference A_{c3} temperature. This indicates a rapid bcc-to-fcc transformation upon heating, as observed in ART700-10.

However, residual α remains detectable at the end of the heating ramp for all target temperatures, as shown by the enlarged α_{110} regions in Fig. 9b, d, and f. The Rietveld-refined phase fractions at the end of rapid heating confirm incomplete austenitization. At 850°C, 900°C, and 950°C, the γ fractions are f_γ = 92.33 ± 0.61, 96.31 ± 0.72, and 97.97 ± 1.47 wt.%, while the corresponding α fractions are f_α = 7.67 ± 0.38, 3.68 ± 0.39, and 2.03 ± 0.29 wt.%, respectively. Based on the defined threshold of $f_\alpha \leq 1$ wt.%, none of the FA treatments from the ART700-60 initial state reaches near-complete bcc-

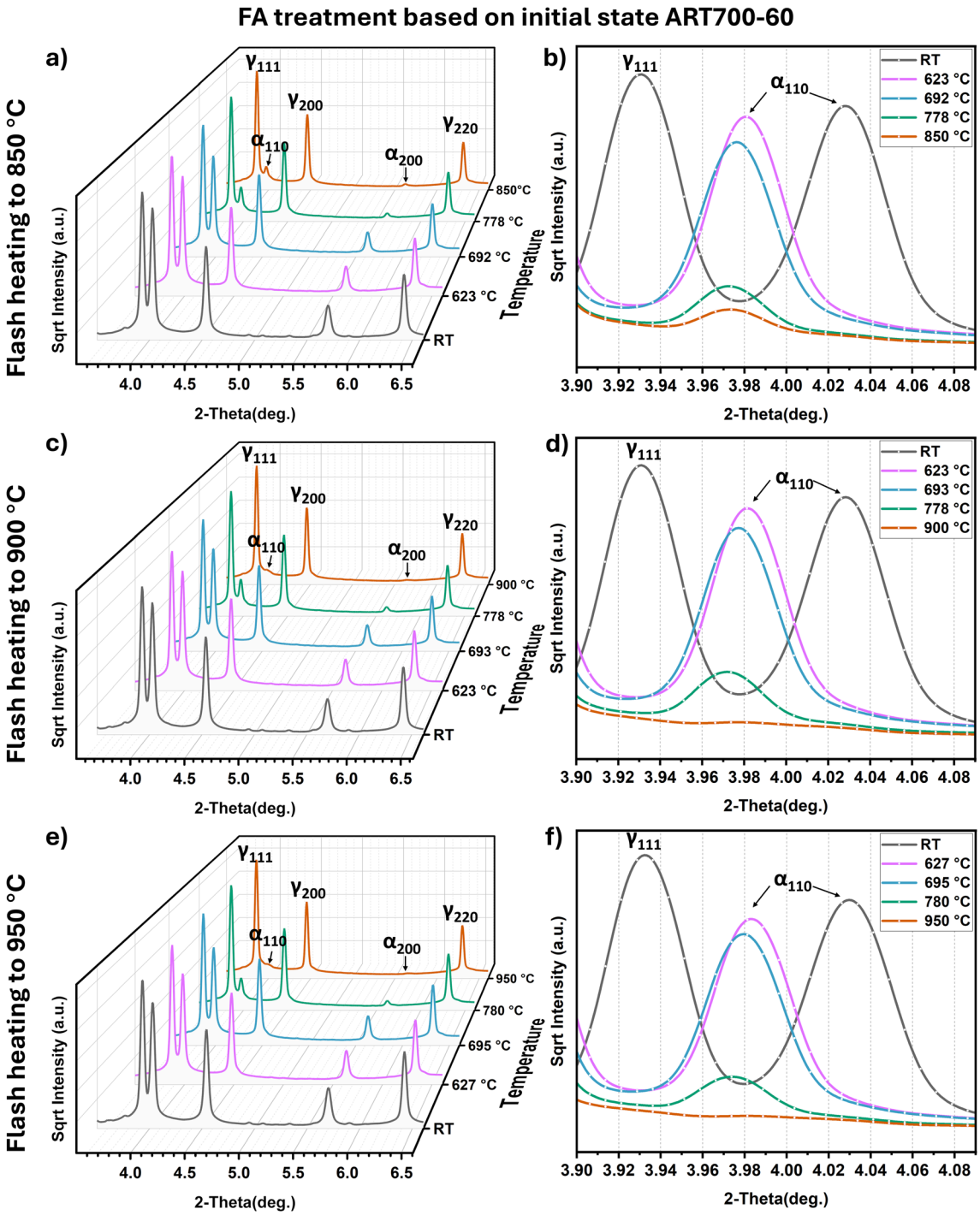

Fig. 9. In situ SYXRD results show microstructural evolution and phase transformation of ART700-60 during rapid heating in FA at 100°C/s from room temperature (RT) to FA temperatures of 850°C (a, b), 900°C (c, d), and 950°C (e, f). (a, c, and e) Waterfall plots of the diffraction profiles in the 2θ range 3.5° to 6.6°. (b, d, and f) Enlarged views of γ_{111} and α_{110}, highlighting the progressive decrease in α_{110} intensity during rapid heating.

to-fcc transformation during rapid heating alone over the 850–950°C range. Thus, exceeding the reference A_{c3} determined under slow-heating conditions is insufficient at 100°C/s without holding.

Figure 10 presents in situ SYXRD results for ART700-60 during isothermal holding after rapid heating to 850°C, 900°C, and 950°C, with $t = 0$ defined as the moment the target FA temperature is reached. Selected phase fractions are listed in Table S-II.

As in ART700-10, residual α remaining after rapid heating decreases rapidly within the first seconds of

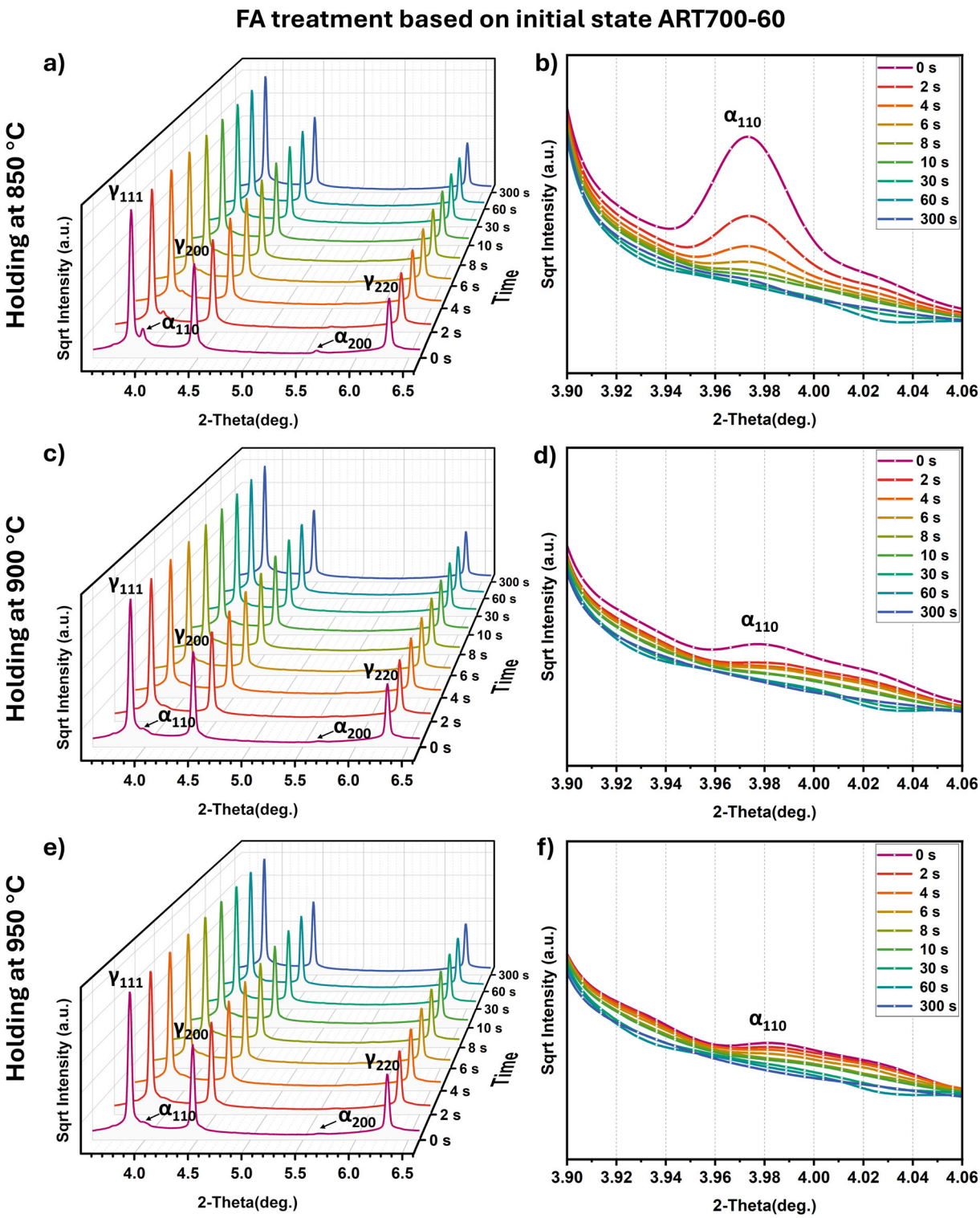

Fig. 10. In situ SYXRD results show microstructural evolution and phase transformation of ART700-60 during isothermal holding after rapid heating in FA to 850°C (a, b), 900°C (c, d), and 950°C (e, f). (a, c, and e) Waterfall plots of the diffraction profiles in the 2θ range 3.5° to 6.6°, showing the time-dependent evolution of bcc (α) and fcc (γ) reflections during holding. (b, d, and f) Enlarged views around the α_{110} reflection.

holding, followed by slower changes once its fraction becomes small. At 850°C, f_α decreases from 7.67 ± 0.38 wt.% at t = 0 to 0.97 ± 0.14 wt.% after 8 s, while f_γ increases to 99.03 ± 1.61 wt.%, reaching the defined threshold of $f_\alpha \leq 1$ wt.% after ~ 8 s. At 900°C, f_α decreases from 3.68 ± 0.39 wt.% to 1.01 ± 0.15 wt.% after 4 s, achieving the threshold within refinement uncertainty. At 950°C, f_α

decreases from 2.03 ± 0.29 wt.% to 1.08 ± 0.17 wt.% after 2 s. Taken together, the in situ SYXRD results show that rapid heating at 100°C/s strongly promotes austenite formation but does not complete the bcc-to-fcc transformation in either of the ART initial states. Near-full austenitization is achieved only after a short isothermal holding step, with the required holding time decreasing as the FA temperature increases.

DISCUSSION

Effect of Initial ART Microstructure on Phase Transformation Kinetics During Flash Austenitization

Figure 11 compares the austenitization kinetics of the two initial ART states during FA. At room temperature, ART700-60 contains 64.58 ± 0.65 wt.% fcc, compared with 56.71 ± 0.69 wt.% in ART700-10, and exhibits a more equiaxed fcc/bcc morphology (Fig. 3 and Table II). The characteristic microstructural length scales, however, are similar. The mean fcc equivalent circular diameter increases only from 0.30 ± 0.18 μm in ART700-10 to 0.35 ± 0.23 μm in ART700-60, while the mean bcc equivalent circular diameter changes from 0.42 ± 0.39 to 0.44 ± 0.34 μm. The LAGB/HAGB fractions are also nearly identical, at 49.60/50.40% for ART700-10 and 49.55/50.45% for ART700-60. Extending the ART holding time from 10 min to 60 min therefore changes the phase fractions and morphology more than the average grain size or boundary character distribution. Both ART states exhibit Mn partitioning from bcc to fcc, but the degree of partitioning differs. The STEM-TKD-EDS results in Fig. 4 show Mn-enriched fcc regions adjacent to relatively Mn-depleted bcc regions in both conditions. ART700-60 contains more strongly Mn-enriched pre-existing austenite, whereas the sampled bcc regions in the two conditions have similar average Mn concentrations. This phase-specific Mn distribution is consistent with previous observations of Mn partitioning to reverted fcc during ART of medium-Mn steels.[14–17,41–43] Because FA involves only a few seconds of high-temperature exposure, long-range Mn homogenization remains limited during rapid heating and short holding.[27,28]

Although the two ART states differ in initial phase fraction, morphology, and the degree of Mn enrichment in fcc, their characteristic phase dimensions, boundary-character distributions, and Mn concentrations in the bcc regions are comparable. Both states also contain abundant pre-existing austenite and numerous bcc/fcc interfaces. Existing bcc/fcc interfaces provide growth fronts, while grain and phase boundaries and carbide-associated regions provide potential sites for further fcc nucleation.[29] These similarities provide comparable conditions for the transformation of the remaining bcc, whereas extending ART primarily changes the initial austenite fraction and the absolute amount of bcc requiring transformation.

The dilatometry and in situ SYXRD results support this interpretation. The two ART states transform over comparable temperature ranges during rapid heating, although ART700-10 shows a more pronounced high-temperature transformation segment because it contains more bcc before FA. As shown in Fig. 11a, ART700-60 retains a higher absolute fcc fraction near the reference A_{c1} temperature because it begins with more fcc. ART700-10 subsequently undergoes a larger absolute increase in fcc fraction because more bcc is available for transformation. As a result, the phase fraction difference between the two initial states becomes smaller as the temperature increases. Between the reference A_{c1} and A_{c3} temperatures, the fcc fractions increase rapidly in both ART states,

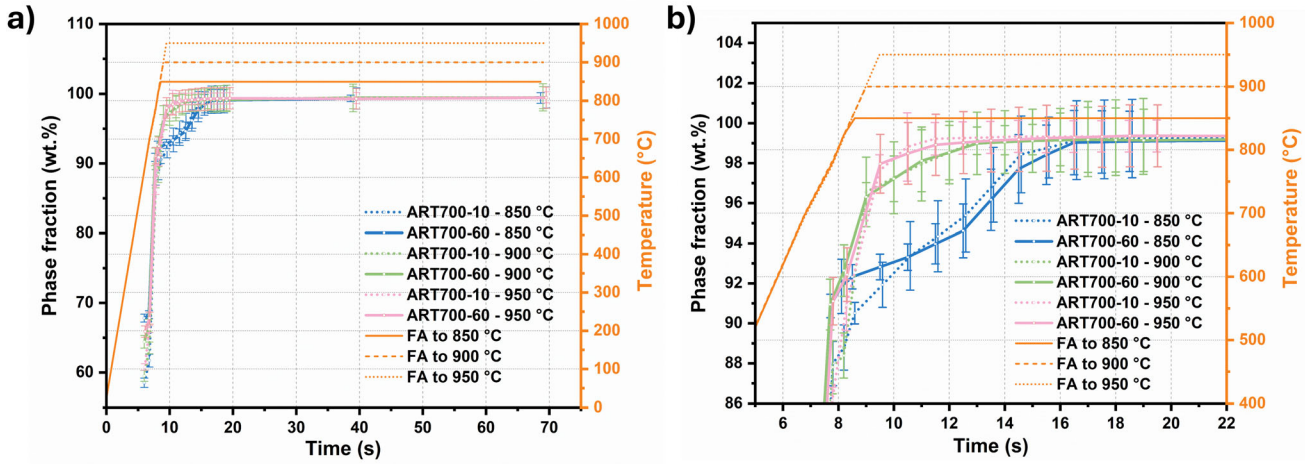

Fig. 11. Comparison of austenite (γ) formation kinetics during flash austenitization (FA) for two initial ART states at FA temperatures of 850°C, 900°C, and 950°C. (a) γ-Phase fraction (in wt.%) as a function of time for ART700-10 and ART700-60. Dash-dotted curves represent ART700-10, solid curves represent ART700-60, and the orange curves show the corresponding temperature-time profiles. (b) Enlarged view of the late heating ramp and holding stage.

with broadly comparable slopes within the refinement uncertainty.

To account for the different initial bcc fractions, the normalized fraction of the initial bcc transformed by the end of the heating ramp was calculated as

$$X_{\alpha,\mathrm{ramp}} = \frac{f_{\alpha,\mathrm{RT}} - f_{\alpha,\mathrm{end\ ramp}}}{f_{\alpha,\mathrm{RT}}} \quad (2)$$

where $f_{\alpha,\mathrm{RT}}$ is the initial bcc fraction at room temperature before FA, and $f_{\alpha,\mathrm{end\ ramp}}$ is the residual bcc fraction when the target FA temperature is reached. For ART700-10, $X_{\alpha,\mathrm{ramp}}$ is approximately 78%, 92%, and 95% for FA to 850°C, 900°C, and 950°C, respectively. For ART700-60, the corresponding values are approximately 79%, 90%, and 94%. Although ART700-60 retains a higher absolute fcc fraction because of its higher initial austenite content, the normalized fraction of initial bcc transformed during the heating ramp is comparable for the two ART states. The normalized results show that extending the ART holding time changes the initial fcc/bcc phase fractions and the absolute amount of bcc requiring transformation, while the fraction of the initial bcc transformed during the heating ramp remains comparable within the investigated conditions.

At the reference A_{c3} temperature (776°C), none of the samples has reached the defined 1 wt.% completion threshold, as shown in Fig. 11b. This indicates that the effective completion temperature under rapid heating is higher than the A_{c3} value determined under slow-heating conditions. This shift is consistent with the heating-rate dependence of the critical transformation temperatures and the limited time available for interface migration, solute redistribution, and carbide dissolution.[50–52] Above the reference A_{c3} and before the target FA temperature is reached, the austenite formation rate decreases for all conditions, marking the transition toward the slow final-stage regime discussed in the "Coupled Effects of FA Temperature and Holding Time on Austenitization Kinetics" section.

The influence of the initial ART state during subsequent holding depends on the target FA temperature. At 900°C and 950°C, rapid heating leaves only approximately 2–4 wt.% residual bcc in either initial state. Both ART states therefore begin holding from comparable phase states, and the holding curves mainly describe the final transformation of a small residual bcc fraction. This convergence of the end-of-ramp phase state explains why the influence of the initial ART condition becomes less pronounced at 900°C and 950°C. At 850°C, approximately 8–10 wt.% bcc remains at the beginning of holding. The early holding stage therefore still involves concurrent nucleation of new fcc and growth of pre-existing fcc. Under this condition, differences in the initial bcc fraction and morphology remain visible for longer.

Overall, ART700-10 and ART700-60 are not equivalent initial states. ART700-60 contains a higher austenite fraction, a more equiaxed phase morphology, and more strongly Mn-enriched pre-existing austenite, whereas ART700-10 contains more bcc and undergoes a larger absolute increase in austenite fraction during FA. However, their characteristic phase dimensions, boundary-character distributions, and Mn concentrations in the bcc regions are comparable. As the FA temperature increases, more than 90% of the initial bcc transforms during the heating ramp, and the residual bcc fractions of the two states converge. The influence of the initial ART condition is less apparent at 900°C and 950°C but remains more evident at 850°C.

Coupled Effects of FA Temperature and Holding Time on Austenitization Kinetics

Figure 11b shows that the transformation behavior during isothermal holding depends strongly on the austenitization progress already completed during the heating ramp. For ART700-10, the residual bcc fraction at the start of holding decreases from 9.49 ± 0.39 wt.% at 850°C to 3.44 ± 0.59 wt.% at 900°C and 2.38 ± 0.48 wt.% at 950°C. For ART700-60, the corresponding fractions are 7.67 ± 0.38, 3.68 ± 0.39, and 2.03 ± 0.29 wt.%, respectively. Isothermal holding therefore begins with different residual-bcc fractions and different progress of the bcc-to-fcc transformation. Increasing the target FA temperature does not merely accelerate an otherwise identical isothermal transformation. It shifts a larger fraction of austenitization into the rapid heating ramp and therefore changes both the residual bcc fraction and the transformation stage at the beginning of holding. At 850°C, holding begins while a substantial bcc fraction remains, whereas at 900°C and 950°C, holding begins directly in the final stage of austenitization.

At 850°C, the phase fraction curve retains a visible S-shaped character, with an initial acceleration period followed by a progressive decrease in transformation rate as austenitization approaches completion. This behavior is consistent with a nucleation and growth-type transformation during the holding stage.[53] Both ART states contain pre-existing austenite and numerous bcc/fcc interfaces before FA. New austenite may therefore continue to nucleate at favorable sites, such as bcc grain boundaries and carbide/matrix interfaces, while pre-existing austenite grows through migration of existing bcc/fcc interfaces.[29,52,54] As austenitization proceeds, readily transformable bcc regions and favorable nucleation sites are progressively depleted, while growing austenite regions are expected to impinge. The remaining bcc consequently becomes smaller and more isolated, and additional nucleation contributes progressively less to the phase fraction change. The slow final-stage austenitization is therefore interpreted as a growth-

dominated regime in which further austenite formation proceeds mainly through migration of existing bcc/fcc interfaces.[53–56]

Retained chemical heterogeneity may additionally delay the final-stage transformation. The STEM-TKD-EDS results in Fig. 4 establish phase-specific Mn partitioning in the ART initial states, with Mn-enriched austenite adjacent to relatively Mn-depleted bcc. Because substitutional Mn diffusion is slow, and previous studies on MMnSs have shown that rapid heating at 100°C/s and short high-temperature exposure do not fully homogenize ART-induced Mn heterogeneity, part of the measured Mn distribution is expected to remain during FA.[27,28,56] Since Mn stabilizes austenite, local Mn variations can produce differences in austenite stability and in the chemical driving force for the bcc-to-fcc transformation. Regions with more favorable local chemical conditions are expected to transform earlier, whereas Mn-lean bcc regions with a lower local driving force for austenite formation may persist into the final stage. Migration of bcc/fcc interfaces across local Mn gradients may additionally require Mn redistribution near the moving interface, which is limited by the low diffusivity of Mn during the short FA cycle.[17,41–43] Continued carbide dissolution and short-range C redistribution may further modify the local chemical conditions.[50,57] In short, the slow final-stage austenitization is attributed to the progressive depletion of readily transformable bcc regions and favorable austenite nucleation sites, as well as the slow transformation of a small, isolated, and chemically heterogeneous residual bcc fraction.

Figure 12a and b compares the final stages using the normalized holding time $t_N = t–t_{99\%}$, where $t_{99\%}$ is the holding time at which $f_\gamma > 99$ wt.% ($f_\alpha < 1$ wt.%) is reached. For both ART states, the 900°C and 950°C curves follow a similar final austenitization path as they approach the threshold, indicating comparable final-stage transformation rates within the refinement uncertainty. Both conditions have already entered the final stage of austenitization before holding begins, although the residual bcc fraction is higher at 900°C than at 950°C. The longer absolute holding time at 900°C therefore mainly reflects the larger residual bcc fraction that must transform before the near-completion criterion is reached rather than a clearly slower final-stage transformation rate. By contrast, the 850°C treatments begin holding with approximately 8–10 wt.% residual bcc and include an earlier stage of continued austenite nucleation and growth before approaching the final stage of austenitization.

These results show that the required holding time cannot be explained simply in terms of faster or slower isothermal transformation kinetics. Instead, it is determined by the complete thermal path, because it reflects both the transformation achieved during rapid heating and the subsequent evolution of the residual bcc during holding. Increasing the FA temperature primarily shifts a larger fraction of austenitization into the rapid heating ramp so that holding begins with less residual bcc and at a more advanced stage of transformation. The residual bcc fraction after rapid heating consequently provides a direct quantitative link between the heating ramp and the required holding step. Neither the A_{c3} value determined under slow-heating conditions nor the nominal FA temperature alone is sufficient to determine the holding time required for near-complete austenitization.

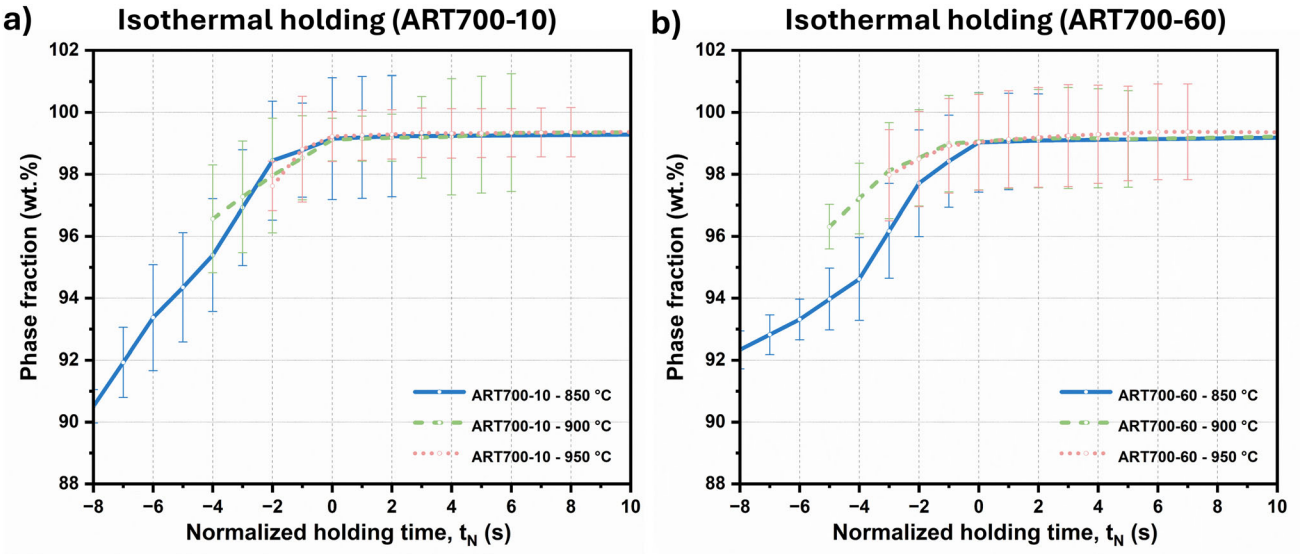

Fig. 12. Normalized austenite (γ) phase fraction (in wt.%) evolution during isothermal holding at 850°C, 900°C, and 950°C for (a) ART700-10 and (b) ART700-60. The γ phase fractions were obtained by Rietveld refinement of the in situ SYXRD patterns, and the error bars represent the corresponding refinement uncertainties. The normalized holding time is defined as $t_N = t–t_{99\%}$, where $t_{99\%}$ is the holding time at which $f_\gamma > 99$ wt.% is reached. Thus, $t_N < 0$ represents the approach to the 99 wt.% γ threshold, and $t_N > 0$ corresponds to the subsequent near-plateau region.

The process design objective of FA in MMnSs is to complete austenitization within a short thermal cycle while limiting prior-austenite grain growth and homogenization of the Mn heterogeneity introduced by ART. The target temperature and holding time must therefore be selected together, because a lower peak temperature does not necessarily correspond to a lower overall thermal exposure if a substantially longer holding time is required. Heating to 850°C leaves 7.67–9.49 wt.% residual bcc and requires approximately 8 s of holding. The lower peak temperature is therefore accompanied by a relatively long isothermal exposure. Heating to 950°C reduces the residual bcc fraction to 2.03–2.38 wt.% and the required holding time to approximately 2 s but imposes the highest peak temperature, which may increase Mn homogenization and prior austenite grain growth.[27,52,58] The total effect on solute redistribution and grain growth cannot be inferred from holding time alone because both processes depend strongly on temperature and duration.

The 900°C condition provides an intermediate combination within the investigated process window. Rapid heating to 900°C reduces the residual bcc fraction to 3.44–3.68 wt.%, and the near-completion criterion is reached after approximately 4 s of holding. At a heating rate of 100°C/s, increasing the target temperature from 850°C to 900°C adds approximately 0.5 s to the heating ramp but reduces the required holding time by approximately 4 s. A further increase from 900°C to 950°C adds another approximately 0.5 s to the heating ramp and reduces the holding time by approximately 2 s, while the final-stage austenitization remains similar. Thus, increasing the target temperature from 900°C to 950°C primarily reduces the residual bcc fraction at the beginning of holding without producing clearly different final-stage kinetics. However, the higher FA temperature may promote more substitutional solute redistribution. Within the investigated FA temperatures, 900°C appears to provide a favorable compromise during flash austenitization, limiting the required holding time and avoiding the higher holding temperature.

CONCLUSION

Using dilatometry-integrated in situ SYXRD, this study quantified the bcc-to-fcc transformation during heating at 100°C/s, followed by a short isothermal hold at 850–950°C, for two ART initial states. Near-complete austenitization was defined by $f_\alpha \leq 1$ wt.% as a quantitative criterion. Neither passing the reference A_{c3} temperature nor reaching target FA temperatures during rapid heating was sufficient to satisfy this criterion.

The main conclusions are as follows:

- Rapid heating and isothermal holding form a kinetically coupled flash austenitization process, and the required holding time is therefore thermal-path dependent. Increasing the FA temperature shifts a larger fraction of the bcc-to-fcc transformation into the heating ramp, so that holding begins with less residual bcc and already at a late austenitization stage.
- Extending ART from 10 min to 60 min changes the initial austenite fraction, phase morphology, and Mn enrichment of austenite but has only a limited effect on the transformation progress during rapid heating. The comparable phase dimensions, boundary-character distributions, and Mn concentrations in the bcc regions provide similar conditions for transformation of the remaining bcc.
- The austenitization mechanism during the isothermal holding stage changes as austenitization progresses at the beginning of holding stage. At 850°C, a substantial bcc fraction remains, and the behavior retains a nucleation-and-growth character, whereas at 900°C and 950°C, holding begins directly in a growth-dominated final stage governed mainly by migration of existing bcc/fcc interfaces. The similar austenitization kinetics at 900°C and 950°C indicate that the final stage of austenitization is less sensitive to FA temperature.

Therefore, FA parameters can be selected by considering both the transformation achieved during rapid heating and the additional holding time required to reach near-complete austenitization. This approach moves FA design beyond empirical peak-temperature selection and provides a quantitative basis for balancing transformation completion against high-temperature exposure. Within the investigated temperature range and heating rate, 900°C appears to provide a favorable intermediate condition because most austenitization is completed during heating, the required holding time is limited to approximately 4 s, and the higher peak temperature is avoided. Future work will compare the post-FA Mn distribution, prior-austenite grain size, and mechanical properties to determine an optimum processing condition.

SUPPLEMENTARY INFORMATION

The online version contains supplementary material available at https://doi.org/10.1007/s11837-026-08740-5.

ACKNOWLEDGEMENTS

The authors gratefully acknowledge Deutsches Elektronen-Synchrotron (DESY, Hamburg, Germany) and the staff of beamline P07 at PETRA III, with special thanks to Dr. Emad Maawad for assistance during the X-ray diffraction experiments. Financial support from the Deutsche Forschungs-

gemeinschaft (DFG, German Research Foundation) under grant no. 490856143 is gratefully acknowledged.

FUNDING

Open Access funding enabled and organized by Projekt DEAL. Deutsche Forschungsgemeinschaft, 490856143, Daniel Schneider and Wenwen Song.

DATA AVAILABILITY

The data that support the findings of this study are available from the corresponding author upon reasonable request.

CONFLICT OF INTEREST

The authors declare that they have no conflict of interest.

OPEN ACCESS

REFERENCES

1. M.F.W. Chowdhury, C.V. Tapia-Bastidas, J. Hoschke, J. Venezuela, and A. Atrens, *Int. J. Hydrogen Energy* 102, 181 https://doi.org/10.1016/j.ijhydene.2025.01.018 (2025).
2. F. Konert, F. Wieder, J. Nietzke, D. Meinel, T. Böllinghaus, and O. Sobol, *Int. J. Hydrogen Energy* 59, 874 https://doi.org/10.1016/j.ijhydene.2024.02.005 (2024).
3. S. Rahimi, K. Verbeken, T. Depover, and E. Proverbio, *Eng. Fail. Anal.* 167, 108956 https://doi.org/10.1016/j.engfailanal.2024.108956 (2025).
4. A.K. Boddorff, Choosing the right stuff: material selection for liquid hydrogen aircraft cryotanks (National Aeronautics and Space Administration, Hampton, VA, 2025), NASA/TM-20250007133, https://ntrs.nasa.gov/citations/20250007133. Accessed 17 July 2026.
5. Y. Kim, S.-H. Lee, M. Park, H. Shim, J.-Y. Kang, and J.-Y. Kim, *Mater. Sci. Eng. A* 914, 147167 https://doi.org/10.1016/j.msea.2024.147167 (2024).
6. C. Reppin, K. Treutler, O. Brätz, A. Gericke, and K.-M. Henkel, *Weld. World*. https://doi.org/10.1007/s40194-025-01973-z (2026).
7. J. Han, J.-H. Nam, and Y.-K. Lee, *Acta Mater.* 113, 1 https://doi.org/10.1016/j.actamat.2016.04.038 (2016).
8. X. Shen, W. Song, S. Sevsek, Y. Ma, C. Hüter, R. Spatschek, and W. Bleck, *Metals* 9, 929 https://doi.org/10.3390/met9090929 (2019).
9. B. Sun, W. Krieger, M. Rohwerder, D. Ponge, and D. Raabe, *Acta Mater.* 183, 313 https://doi.org/10.1016/j.actamat.2019.11.029 (2020).
10. L. Cho, Y. Kong, J.G. Speer, and K.O. Findley, *Metals* 11, 358 https://doi.org/10.3390/met11020358 (2021).
11. M. Stadler, R. Schnitzer, M. Gruber, K. Steineder, and C. Hofer, *Materials* 14, 3362 https://doi.org/10.3390/ma14123362 (2021).
12. G. Park, K. Kim, S. Uhm, and C. Lee, *Mater. Sci. Eng. A* 766, 138401 https://doi.org/10.1016/j.msea.2019.138401 (2019).
13. Y. Cao, C. Luo, L. Zhao, Y. Peng, L. Song, C.-Y. Ma, Z.-L. Tian, M.-L. Zhong, and Y.-J. Wang, *J. Iron Steel Res. Int.* 27, 75 https://doi.org/10.1007/s42243-019-00293-z (2020).
14. X. Shen, H. Qiao, W. Song, and W. Bleck, *Steel Res. Int.* 94, 2300145 https://doi.org/10.1002/srin.202300145 (2023).
15. B. Hu, X. Shen, Q. Guo, Q. Wen, X. Tu, C. Ding, F. Ding, W. Song, and H. Luo, *J. Mater. Sci. Technol.* 126, 60 https://doi.org/10.1016/j.jmst.2022.04.003 (2022).
16. Z.J. Xie, C.J. Shang, S.V. Subramanian, X.P. Ma, and R.D.K. Misra, *Scr. Mater.* 137, 36 https://doi.org/10.1016/j.scriptamat.2017.05.002 (2017).
17. J.T. Benzing, A. Kwiatkowski Da Silva, L. Morsdorf, J. Bentley, D. Ponge, A. Dutta, J. Han, J.R. McBride, B. Van Leer, B. Gault, D. Raabe, and J.E. Wittig, *Acta Mater.* 166, 512 https://doi.org/10.1016/j.actamat.2019.01.003 (2019).
18. B. Sun, W. Lu, B. Gault, R. Ding, S.K. Makineni, D. Wan, C.-H. Wu, H. Chen, D. Ponge, and D. Raabe, *Nat. Mater.* 20, 1629 https://doi.org/10.1038/s41563-021-01050-y (2021).
19. X.T. Deng, X.L. Li, L. Huang, and Z.D. Wang, *Mater. Sci. Forum* 993, 520 https://doi.org/10.4028/www.scientific.net/MSF.993.520 (2020).
20. R.A. Grange, *Metall. Trans.* 2, 65 https://doi.org/10.1007/BF02662639 (1971).
21. Y. Liu, M. Zhang, H. Li, X. Zhang, S. Qu, B. Fernandez Hernandez, and X. Han, *Mater. Sci. Eng. A* 947, 149213 https://doi.org/10.1016/j.msea.2025.149213 (2025).
22. V. Sinha, M. Gonzales, and E.J. Payton, *Metallogr. Microstruct. Anal.* 14, 404 https://doi.org/10.1007/s13632-024-01162-2 (2025).
23. P. Wen, B. Hu, J. Han, and H. Luo, *J. Mater. Sci. Technol.* 97, 54 https://doi.org/10.1016/j.jmst.2021.04.035 (2022).
24. M. Wang, J. Chang, H. Wu, Z. Mi, Y. Wu, and Q. Zhang, *Metals* 14, 1006 https://doi.org/10.3390/met14091006 (2024).
25. S. Huang, L. Li, H. Ye, X. Xing, J. Ouyang, Z. Li, X. Zhang, S. Chen, and Z. Peng, *Materials* 18, 2488 https://doi.org/10.3390/ma18112488 (2025).
26. M. Gaggiotti, L. Albini, P. Di Nunzio, A. Di Schino, G. Stornelli, and G. Tiracorrendo, *Metals* 12, 1313 https://doi.org/10.3390/met12081313 (2022).
27. Y. Wang, R. Ding, C. Franke, T. Li, X. Rong, P. Wen, Z. Yang, and H. Chen, *Scr. Mater.* 242, 115923 https://doi.org/10.1016/j.scriptamat.2023.115923 (2024).
28. X. Wan, G. Liu, Z. Yang, and H. Chen, *Scr. Mater.* 198, 113819 https://doi.org/10.1016/j.scriptamat.2021.113819 (2021).
29. V.A. Esin, B. Denand, Q. Le Bihan, M. Dehmas, J. Teixeira, G. Geandier, S. Denis, T. Sourmail, and E. Aeby-Gautier, *Acta Mater.* 80, 118 https://doi.org/10.1016/j.actamat.2014.07.042 (2014).
30. N. Fonstein, *Advanced High Strength Sheet Steels* (Springer International Publishing, Cham, 2015), p 275–295. https://doi.org/10.1007/978-3-319-19165-2_8.
31. M. Storm, P. Staron, and C. Krywka, *J. Appl. Crystallogr.* 58, 1476 https://doi.org/10.1107/S160057672500398X (2025).
32. N. Schell, A. King, F. Beckmann, T. Fischer, M. Müller, and A. Schreyer, *Mater. Sci. Forum* 772, 57 https://doi.org/10.4028/www.scientific.net/MSF.772.57 (2013).
33. D.K. Smith, J. Fiala, and E. Ryba, *Powder Diffr.* 8, 252 https://doi.org/10.1017/S0885715600019497 (1993).
34. L. Lutterotti, *Acta Crystallogr. A* 56, s54 https://doi.org/10.1107/S0108767300021954 (2000).
35. B.H. Toby, *Powder Diffr.* 21, 67 https://doi.org/10.1154/1.2179804 (2006).

36. L. Yang, X. Wang, C. Du, N. Lu, C. Li, and H. Zhang, *J. Mater. Res. Technol.* 39, 9308 https://doi.org/10.1016/j.jmrt.2025.11.220 (2025).
37. T. Tanaka, N. Maruyama, N. Nakamura, and A.J. Wilkinson, *Acta Mater.* 195, 728 https://doi.org/10.1016/j.actamat.2020.06.017 (2020).
38. Q. Luo, *J. Mater. Eng. Perform.* 25, 2170 https://doi.org/10.1007/s11665-016-2053-0 (2016).
39. F. Forouzan, R. Surki Aliabad, A. Hedayati, N. Hosseini, E. Maawad, N. Blasco, and E. Vuorinen, *Materials* 16, 1557 https://doi.org/10.3390/ma16041557 (2023).
40. H. Nasr El-Din, E.A. Showaib, N. Zaafarani, and H. Refaiy, *Int. J. Mech. Mater. Eng.* 12, 3 https://doi.org/10.1186/s40712-017-0071-9 (2017).
41. A. Mehrabi, H. Zurob, I.-E. Benrabah, and J.R. McDermid, *J. Mater. Res. Technol.* 30, 2158 https://doi.org/10.1016/j.jmrt.2024.03.241 (2024).
42. I.R. Souza Filho, A. Kwiatkowski Da Silva, M.J.R. Sandim, D. Ponge, B. Gault, H.R.Z. Sandim, and D. Raabe, *Acta Mater.* 166, 178 https://doi.org/10.1016/j.actamat.2018.12.046 (2019).
43. Q. Guo, H.-W. Yen, H. Luo, and S.P. Ringer, *Acta Mater.* 225, 117601 https://doi.org/10.1016/j.actamat.2021.117601 (2022).
44. S. Pashangeh, H.R. Karimi Zarchi, S.S. Ghasemi Banadkouki, and M.C. Somani, *Metals* 9, 492 https://doi.org/10.3390/met9050492 (2019).
45. Y. Zhang, P. Lai, H. Jia, X. Ju, and G. Cui, *Metals* 9, 94 https://doi.org/10.3390/met9010094 (2019).
46. Y. Ma, *Mater. Sci. Technol.* 33, 1713 https://doi.org/10.1080/02670836.2017.1312208 (2017).
47. A. Skowronek, A. Grajcar, C. Garcia-Mateo, J.A. Jiménez, and R.H. Petrov, *Metall. Mater. Trans. A* 54, 1443 https://doi.org/10.1007/s11661-023-06998-x (2023).
48. P. Mayr, T.A. Palmer, J.W. Elmer, E.D. Specht, and S.M. Allen, *Metall. Mater. Trans. A* 41, 2462 https://doi.org/10.1007/s11661-010-0371-7 (2010).
49. L. León-Reina, M. García-Maté, G. Álvarez-Pinazo, I. Santacruz, O. Vallcorba, A.G. De La Torre, and M.A.G. Aranda, *J. Appl. Crystallogr.* 49, 722 https://doi.org/10.1107/S1600576716003873 (2016).
50. S. Papaefthymiou, M. Bouzouni, and R.H. Petrov, *Metals* 8, 646 https://doi.org/10.3390/met8080646 (2018).
51. J. Moravec, I. Nováková, and J. Vondráček, *Manuf. Technol.* 20, 217 https://doi.org/10.21062/mft.2020.024 (2020).
52. A. Eggbauer, M. Lukas, G. Ressel, P. Prevedel, F. Mendez-Martin, J. Keckes, A. Stark, and R. Ebner, *J. Mater. Sci.* 54, 9197 https://doi.org/10.1007/s10853-019-03527-3 (2019).
53. G.R. Speich, V.A. Demarest, and R.L. Miller, *Metall. Trans. A* 12, 1419 https://doi.org/10.1007/BF02643686 (1981).
54. E.D. Schmidt, E.B. Damm, and S. Sridhar, *Metall. Mater. Trans. A* 38, 244 https://doi.org/10.1007/s11661-006-9029-x (2007).
55. X. Hu, J.J. Mueller, X. Sun, E. De Moor, J.G. Speer, D.K. Matlock, and Y. Ren, *Front. Mater.* 8, 621784 https://doi.org/10.3389/fmats.2021.621784 (2021).
56. G. Liu, Z. Dai, Z. Yang, C. Zhang, J. Li, and H. Chen, *J. Mater. Sci. Technol.* 49, 70 https://doi.org/10.1016/j.jmst.2020.01.051 (2020).
57. J.J. Mueller, X. Hu, X. Sun, Y. Ren, K. Choi, E. Barker, J.G. Speer, D.K. Matlock, and E. De Moor, *Mater. Des.* 203, 109598 https://doi.org/10.1016/j.matdes.2021.109598 (2021).
58. D.K. Matlock, S. Kang, E. De Moor, and J.G. Speer, *Mater. Charact.* 166, 110397 https://doi.org/10.1016/j.matchar.2020.110397 (2020).